CHEMISTRY OF MATERIALS

ARTICLE

pubs.acs.org/cm

Crystal Chemistry and Electronic Structure of the Photovoltaic Buffer Layer, $(In_{1-x}Al_x)_2S_3$

A. Lafond,*,† X. Rocquefelte,*,† M. Paris,† C. Guillot-Deudon,† and V. Jouenne†

†Institut des Matériaux Jean Rouxel (IMN), Université de Nantes, CNRS 2, rue de la Houssinière, BP 32229, 44322 Nantes cedex 03, France

Supporting Information

ABSTRACT: We have investigated the effects of the aluminum substitution in In_2S_3 using an approach that combines X-ray diffraction, nuclear magnetic resonance (NMR) experiments, and density functional theory (DFT) calculations. For the very first time, an understanding of the evolution of the local structure in this family with Al-content is reached based on the synergy of these three techniques. In particular, the comparison of the measured and simulated ^{27}Al NMR quadrupolar constants allows an unambiguous attribution of the Al-sites in the investigated $(In_{1-x}Al_x)_2S_3$ compounds ($0 \leq x \leq 0.185$). It shows that for high Al-contents a new tetrahedral site (Td(4a)) is occupied, leading to a tetragonal to cubic modification. The present paper provides a definite explanation of the band gap reduction upon the aluminum substitution in In_2S_3, which is directly related to the occupation of the Td(4a) site. The present results could help to improve the performances of solar cells using In_2S_3-based compounds as alternative buffer layers.

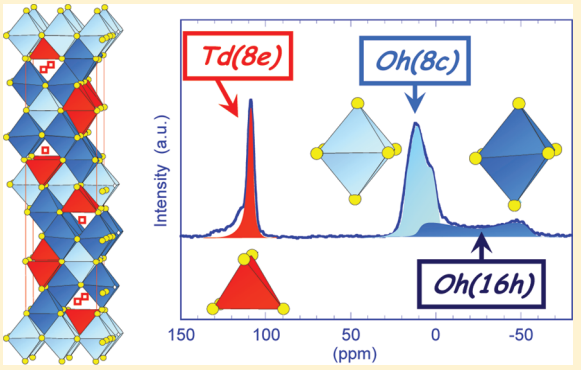

KEYWORDS: ^{27}Al NMR, density functional theory, X-ray diffraction, crystal structure, indium aluminum sulfide, photovoltaics

1. INTRODUCTION

The industrial production of solar modules based on the Cu(In,Ga)Se_2 (CIGS)-based thin-film photovoltaic (PV) technology is now underway, but there is room for improvements. In particular, the CIGS industrial modules are equipped with a thin CdS buffer layer. While the use of CdS buffer layer leads to PV cells with solar conversion efficiency greater than 20% in laboratory,[1] it also exhibits some drawbacks, namely (i) the too small band gap of CdS ($E_g \approx 2.4$ eV) leads to absorption losses and then a reduction of the quantum efficiency of the solar cell at short wavelengths, (ii) the toxicity of Cd, and (iii) the use of chemical bath deposition (CBD) technique, leading to interrupt the vacuum growth process.

Therefore, many efforts are going on to replace the (CBD)-CdS buffer layer by Cd-free compounds. Among the alternative buffer materials, In_2S_3-based compounds are performing very well.[2−6] However, the band gap of In_2S_3 (~2.0 eV)[7−9] is too small to avoid important absorption losses. In order to raise the band gap value, two different indium sulfide derivatives have been envisioned, namely $In_2S_{3-3x}O_{3x}$ and $(In_{1-x}Al_x)_2S_3$. By substituting part of the oxygen for sulfur, or aluminum for indium, E_g is expected to increase due to the stronger ionicity of the resulting compound. Using such a strategy, Barreau et al. were able to tune the band gap up to 2.9 eV when varying x from 0 to 0.14 in $In_2S_{3-3x}O_{3x}$.[10] In contrast, although the substitution of aluminum for indium in $(In_{1-x}Al_x)_2S_3$ has been demonstrated up to $x = 0.5$,[11] the band gap does not increase so much with x; it sharply increases from 2.00 to 2.20 eV when the x is raised up to 0.03; however it then levels off to 2.12 ± 0.02 eV for higher Al contents.[12] The purpose of the present paper is to provide a definite explanation of such band gap variation based on an accurate characterization of the structural evolution upon the aluminum substitution using a strategy combining X-ray diffraction, NMR spectroscopy, and DFT modeling.

The structure of In_2S_3 is a defect spinel structure with indium vacancies distributed on the tetrahedral sites. At room temperature these vacancies are ordered leading to a tetragonal structure, namely β-In_2S_3, with the space group $I4_1/amd$.[13,14] When the tetrahedral vacancies are randomly distributed (e.g., at higher temperature) the structure undergoes a phase transition toward a cubic form, α-In_2S_3, with the space group Fd-$3m$.[15−17]

A previous X-ray powder diffraction study has shown that the symmetry of the $(In_{1-x}Al_x)_2S_3$ compounds depends on the Al-content, i.e. tetragonal when $x < 0.05$, cubic for $0.1 < x < 0.2$, and finally hexagonal for $x > 0.3$.[18] However, no results on the structural evolution are available for this solid solution which can explain the evolution of the band gap of these compounds.

The In/Al substitution process is expected to be quite complex; aluminum atoms can share tetrahedral and/or octahedral sites with indium atoms and could impact the In/vacancies distribution leading to structural modifications. Because these modifications occur for low aluminum contents, the X-ray diffraction technique, including single crystal diffraction, is not sensitive enough to locate Al atoms in the structure.

Received: June 28, 2011
Revised: September 30, 2011
Published: November 09, 2011

Table 1. Single Crystal Data Collection and Structure Refinement Details

	sample #1	sample #4	sample #6
		Crystal Data	
chemical formula	In_2S_3	$In_{1.94}Al_{0.06}S_3$	$In_{2.33}Al_{0.33}S_4$; $In_{1.75}Al_{0.25}S_3$
space group	$I4_1/amd$	$I4_1/amd$	$Fd\text{-}3m$
a, c (Å)	a = 7.62049(7) c = 32.3603(7)	a = 7.6038(5) c = 32.260(2)	a = 10.6990(7)
V (Å)^3	1880.9(6)	1865.2(6)	1224.7(2)
Z	16	16	8
μ (mm^{-1})	10.94	10.75	10.16
ρ_{calc} (g m^{-3})	4.6083	4.5645	4.3927
crystal size (block) μm	210 - 100 - 67	78 - 70 - 20	15 - 52 - 20
T_{min} T_{max}	0.23/0.52	0.64/0.82	0.23/0.28
no. of meas. ref.	13728	31471	9753
no. of ind. ref.	1426	2969	155
no. of obs. ref I > 2σ(I)	1196	2168	121
R_{int}(obs/all)	4.59/4.89	7.15/8.28	7.9/8.4
range of h ; k; l	−12, 8 ;−12,12 ; −38, 51	−12, 12 ; −12, 12 ; −52, 52	−16, 17 ; −16, 17 ; −16, 17
		Refinement against F^2	
Robs/all	2.29/3.25	3.91/6.57	4.74/6.40
Rwobs/all	6.80/7.55	8.54/10.09	10.86/11.44
S	1.17	1.18	1.57
no. parameters	36	36	8
ρ_{min}; ρ_{max}	1.79/-1.33	1.79/-1.72	2.66/-2.45

Herein, we propose for the very first time an unambiguous identification of the Al-local environment evolution as a function of x in $(In_{1-x}Al_x)_2S_3$, based on a strategy combining X-ray diffraction, ^{27}Al-NMR spectroscopy, and DFT geometry optimization. The so-obtained mechanism of the In/Al substitution in $(In_{1-x}Al_x)_2S_3$ allows us to explain the band gap evolution with x in these compounds.

2. EXPERIMENTAL SECTION

2.1. Synthesis. The compounds were prepared by the solid state reaction of In (Alfa Aesar shot 5N), Al (Alfa Aesar slug 4N), and S(Sigma-Aldrich flake 4N) in the appropriate ratios. The reactants were heated slowly up to 850 °C and held for 1 week, in evacuated sealed silica tubes. Then the samples were ground and reheated to obtain homogeneous powder and crystals. The prepared samples have been labeled using consecutive numbers, sample #1 to sample #7 corresponding to increasing Al content from x = 0 to 0.185.

2.2. Chemical Analyses. The chemical analyses were performed on polished sections of the products embedded in epoxy both with energy dispersive spectrometry (EDS) and wavelength dispersive spectrometry (WDS) using scanning electron microscopes, JEOL 5800LV and Zeiss Merlin FE-SEM, respectively. For all the studied samples, the Al weight percentages are low (Al wt% = 3.4% for x = 0.185). We have then used a highly sensitive analytical method such as WDS. This technique is known for its high efficiency to collect and separate the X-ray signals. The elemental percentages were calculated using calibrated internal standards leading to accurate and precise results. The chemical compositions of the compounds are obtained from the average of 3 to 11 spot analyses depending on the samples. The dispersion of the results is low showing the high homogeneity of the powder samples on a micrometer scale. Average compositions are presented with the powder X-ray diffraction results (part 3.1).

2.3. Powder X-ray Diffraction. Powder X-ray patterns were collected at room temperature on Bruker D8 diffractometer with a Ge (111) monochromator set up in Bragg−Brentano geometry with a Vantec position sensitive detector. The powder patterns were recorded in the 2θ range 10−100° with 0.008° 2θ steps. For sample #3 ($(In_{0.971}Al_{0.029})_2S_3$), a supplementary powder pattern has been collected on the beamline CRISTAL at synchrotron Soleil (France). A monochromatic beam of wavelength 0.62073 Å was used. The sample was loaded in a 0.3 mm diameter glass capillary, which was mounted on a two circle diffractometer equipped with a 21 crystals multianalyzer. The 2θ range was 0−70° with a continuous scan. The full pattern matching refinements were carried out with the help of the JANA2006 program.[19] For all the studied samples, the estimated standard deviations on the unit cell parameters given by the program lead to standard deviations on the unit cell volumes in the range of 0.05−0.2 Å^3. It seems more realistic to use a value of 0.5 A^3. The full pattern matching plot for sample #3 is available as Supporting Information.

2.4. Single Crystal X-ray Diffraction. Single crystal determinations were performed for In_2S_3 (sample #1), $(In_{0.97}Al_{0.03})_2S_3$ (sample #4), and $(In_{0.89}Al_{0.11})_2S_3$ (sample #6). Data collections were carried out on a Bruker-Nonius kappa CCD. A lower symmetry than the actual one was used to ensure redundancy. The recorded images were processed with the programs from Nonius. Details of data collections are summarized in Table 1.

For sample #1 and #4 all the examined crystals were found to be twinned as already mentioned for In_2S_3.[20] The data collection led to a large cubic unit cell with a parameter of about 32.3 Å corresponding to a [601] twinning direction in the direct space with respect to the tetragonal unit cell. The transformation matrix from the large cubic unit cell $a_C \approx$ 32.3 Å to the tetragonal one (a_T, b_T, c_T) is the following one

$$\begin{pmatrix} a_T \\ b_T \\ c_T \end{pmatrix} = \begin{pmatrix} 1/6 & 1/6 & 0 \\ -1/6 & 1/6 & 0 \\ 0 & 0 & 1 \end{pmatrix} \times \begin{pmatrix} a_C \\ b_C \\ c_C \end{pmatrix}$$

All the data processing and the single crystal structure refinements (against F^2) were performed with the JANA2006 program. For all the

dx.doi.org/10.1021/cm201830e |Chem. Mater. 2011, 23, 5168–5176

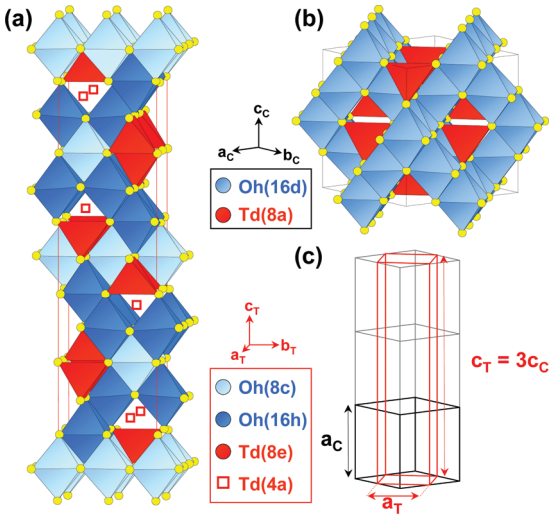

Figure 1. Schematic representation of the crystal structures of (a) β-In_2S_3 (tetragonal symmetry) and (b) α-In_2S_3 (cubic symmetry) and (c) the relation between their respective unit cell parameters. The two octahedral sites of the tetragonal In_2S_3 (16h and 8c Wyckoff positions, in dark-blue and light-blue, respectively) correspond to only one into the cubic In_2S_3 (16d). The disordering of the tetrahedral sites of the tetragonal structure (8e full occupied and 4a empty) leads to the cubic one with the 8a site statistically occupied (sof = 2/3).

samples the absorption corrections, based on the crystal shapes, were optimized using the X shape program and then applied.

2.5. ^{27}Al NMR Measurements. ^{27}Al magic angle spinning (MAS) nuclear magnetic resonance (NMR) spectra were acquired on a Bruker Avance III 500 MHz spectrometer. A 2.5 mm MAS probehead was used for the central-transition MAS spectra. Excitation was done using a $\pi/12$ central-transition selective pulse of 13 kHz radiofrequency (RF) strength. MAS frequency was set to 30 kHz and repetition time to 1 s after checking it was enough to ensure full relaxation. In such conditions, spectra can be considered as quantitative. The ^{27}Al 3Q-MAS spectrum was acquired at a MAS frequency of 14 kHz on a 4 μm MAS probehead using the 3-pulse sequence with Z filter.[21] At RF strength of 100 kHz, the 3Q excitation and reconversion pulses lengths were set to 3.3 and 1.4 μs, respectively. The third pulse duration for signal observation was 4 μs for RF strength of 20 kHz. The ppm scale is referenced to 1M $Al(NO_3)_{3(aq)}$. All spectral decompositions were done using the "dm-fit"[22] NMR freeware package.

2.6. DFT Electronic Band Structure Calculations. Density functional theory (DFT) calculations have been carried out using two different codes: Vienna Ab initio Simulation Package (VASP)[23] for the geometry optimization of the $(In,Al)_2S_3$ atomic structures and the WIEN2k program package[24] for the calculation of the electronic structures, band gap, and electric field gradients (EFG). In both cases, we employed the Perdew-Burke-Ernzerhof (PBE) generalized gradient approximation (GGA) for the exchange and correlation potential.[25]

The parameters used in the VASP calculations are the following. The wave functions are expanded in a plane-wave basis set with kinetic energy below 500 eV. The VASP package is used with the projector augmented wave (PAW) method of Blöchl.[26] The integration in the Brillouin Zone is done by the Methfessel-Paxton method[27] on a set of k-points determined by the Monkhorst-Pack scheme.[28] All the optimizations of atomic coordinates are driven by following a conjugate gradient minimization of the total energy scheme (3.10−2 eV/Å).

The density of states, band gaps, and EFGs are deduced from a self-consistent calculation, using the Full-potential Linearized Augmented Plane Wave (FP-LAPW) method, as embodied in the WIEN2k code.

Table 2. Atomic Coordinates and Equivalent Isotropic Displacement Parameters for In_2S_3 Determined Using the Single-Crystal XRD Data

atom	site	x	y	z	U_{eq} (Å^2)	bond valence[a]
In1	8c	0	0	0	0.0158(2)	3.1
In2	16h	0	−0.01962(7)	0.33246(1)	0.0153(1)	3.06
In3	8e	0	0.25	0.20447(2)	0.0115(1)	3.08
S1	16h	0	−0.0065(2)	0.25086(6)	0.0119(4)	2.16
S2	16h	0	0.0097(2)	0.07835(6)	0.0140(4)	1.90
S3	16h	0	0.0220(2)	0.41312(5)	0.0106(3)	2.09

[a] The bond valence of In, Al, and S have been calculated according to Brown[38] using the valence coefficient for In−S bond from Brese.[39]

The maximum l value in the expansion of the basis set inside the atomic spheres was 12. The convergence of basis set is controlled by a cutoff parameter RMT × K_{max} = 7, where RMT is the smallest atomic sphere radius in the unit cell and K_{max} is the magnitude of the largest k vector. The self-consistency was carried out with the following radii RMT(Al) = 2.2 a.u., RMT(In) = 2.4 a.u., RMT(S) = 2.1 a.u., and GMAX = 12 Bohr^{-1}.

3. RESULTS AND DISCUSSION

According to the already published results,[14−17] the relationships between the unit cell parameters of cubic α-In_2S_3 and tetragonal β-In_2S_3 are as follows: $a_C \approx a_T \times \sqrt{2} \approx c_T/3$ and $V_C \approx V_T \times 2/3$. For simplicity, we will use the following notation in the present paper, Td and Oh for tetrahedral and octahedral, respectively. The indium vacancies in the β-form are ordered; with a fully occupied Td(8e) and an empty Td(4a) sites, while in the α-form, the indium vacancies are randomly distributed with an occupancy factor of 2/3 on the Td(8a) site (see Figure 1).

However, some discrepancies within these published results on the structure of β-In_2S_3 remain. As a consequence, we have decided to reinvestigate the crystal structure of β-In_2S_3. Because the selected single crystal was twinned along the [601] direction, the unit cell used for the data collection was a large cubic unit cell with a = 32.3507 Å. After reducing to the corresponding tetragonal cell, the obtained unit cell parameters were a_T = 7.6251 Å and c_T = 32.3507 Å, which correspond to an ideal ratio of $c/a = 3 \times \sqrt{2}$. These values are very close to those obtained from the powder diffraction pattern. Finally, we decided to use the powder unit cell parameters, a = 7.62049(7) and c = 32.3603(7), for the single crystal refinement. The obtained reliability factors are quite low, R = 2.29 and R_w = 6.80 for 1196 observed reflections and 36 refined parameters. The corresponding Fourier-difference map is featureless (+1.79/−1.33 e/Å^3). In addition, the quality of this crystal structure refinement is supported by the bond valence sums for In sites (see Table 2) which are very close to the expected value of +3 for indium. Finally, the refined structure is in very good agreement with the literature,[13,14] i.e., both the octahedral (Oh(8c) and Oh(16h)) and tetrahedral (Td(8e)) sites are fully occupied meaning an ordered distribution of In^{3+} ions and In-vacancies (V_{In}) along the c axis.

In order to validate our DFT calculations, we carried out a geometry optimization for β-In_2S_3 using the VASP code. As expected, the cell parameters are found to be slightly overestimated (by less than 2%) using the PBE functional, i.e. a_T(DFT) = 7.7572 Å and c_T(DFT) = 32.956 Å, with respect to a_T(XRD) = 7.6205 Å and c_T(XRD) = 32.360 Å. As a corollary,

dx.doi.org/10.1021/cm201830e |Chem. Mater. 2011, 23, 5168–5176

Table 3. Unit Cell Parameters in the $(In_{1-x}Al_x)_2S_3$ Series

	this study				Popovic et al.[b]	
sample	x[a]	a (Å)	c (Å)	V cubic (Å^3)	x	V cubic (Å^3)
#1	0	7.62049(7)	32.3603(7)	1252.8	0	1250.5
#2	0.018(5)	7.60909(9)	32.2987(5)	1246.7	0.077	1243.3
#3	0.029(1)	7.60169(3)[c]	32.26411(14)	1243.2	0.091	1242.0
#4	0.040(2)	7.59470(18)	32.2362(14)	1239.6	0.111	1241.4
#5	0.110(2)	10.7031(2)		1226.1	0.143	1237.0
#6	0.125(5)	10.6921(4)		1222.3	0.200	1230.0
#7	0.185(6)	10.6415(6)		1205.1	0.333	1225.4

[a] The Al-contents (x) have been determined from EDS analyses for sample #2, others from WDS analyses. ESD on x are calculated from the dispersion of results on all the analyzed spots. [b] Our results are compared with the values in reference 18. [c] From synchrotron experiment @ Soleil.

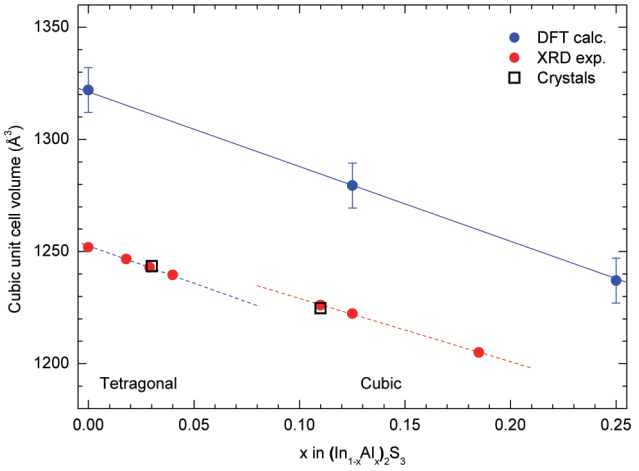

Figure 2. Evolution of the unit cell volume within the $(In_{1-x}Al_x)_2S_3$ series (volumes are based on the cubic unit cell: $V_{Cubic} \approx 2/3 \times V_{Tetra}$). The red circles correspond to the values deduced from the powder X-ray diffraction study, while the open squares give the unit cell volumes of the single crystals of samples #4 and #6. The blue line shows the evolution of the theoretical unit cell volume according to the DFT-calculations with a tetragonal structure model.

In−S distances are slightly overestimated in the present DFT calculations, with optimized average bond lengths of 2.515, 2.656, and 2.664 Å, respectively for Td(8e), Oh(8c), and Oh-(16h) sites. Finally the band gap is significantly underestimated compared to the experimental value of 2.0 eV, with a value E_g(PBE) = 0.9 eV. The present results are very close to a previous GGA investigation, both in terms of structural and band gap parameters.[29]

3.1. Evolution of the Unit Cell Parameters. Let us now consider the effect of the substitution of aluminum for indium on the cell parameters in $(In_{1-x}Al_x)_2S_3$. In 1982, Popovic et al.[18] evidenced that $(In_{1-x}Al_x)_2S_3$ series undergoes a transition from tetragonal ($I4_1/amd$) to cubic ($Fd\bar{3}m$) symmetry for $x > 0.05$. However, in this previous investigation, the compositions of the prepared compounds were not checked by an accurate technique. We have then decided to reinvestigate the evolution of the unit cell parameters along this solid solution by means of X-ray powder diffraction technique combined with accurate elemental

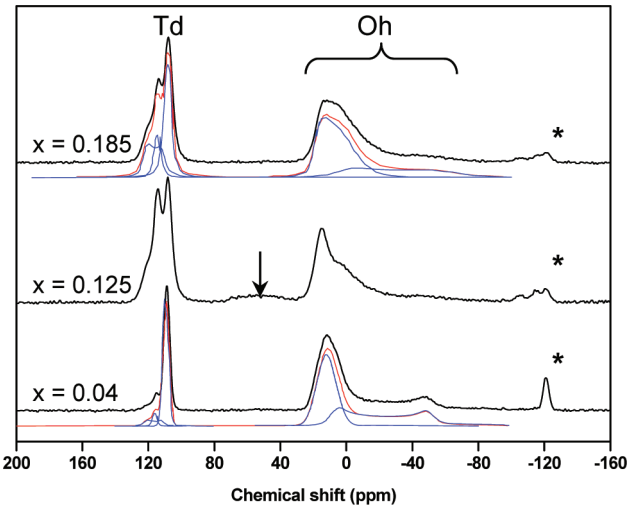

Figure 3. ^{27}Al NMR spectra for samples #4 ($x = 0.04$), #6 ($x = 0.125$), and #7 ($x = 0.185$). The arrow indicates a possible 5-fold coordination. Asterisks denote spinning side bands. In addition the decompositions of the ^{27}Al NMR experimental spectra (in black) for samples #4 and #7 are given; individual lines are in blue while the sums are in red. The calculated spectra are shifted for clarity.

composition analyses. The evolution of the unit cell volume versus x (see Table 3 and Figure 2) is found to be quite regular for $0 \leq x \leq 0.20$ despite the symmetry changes from the tetragonal to the cubic form for $x > 0.05$. The EDS and WDS measurements have evidenced that the aluminum contents in these compounds are often lower than the targeted values. Such an observation could explain the discrepancy observed between present and Popovic et al. values (see Table 3).

In addition, Figure 2 gives DFT optimized unit cell volumes for different Al-compositions. These calculations were carried out using the tetragonal unit cell and progressively replacing 0, 4, 8, 12, and 16 In^{3+} ions by Al^{3+} ions on the Oh(16h) site, i.e. respectively for $x = 0$, 0.125, 0.25, 0.375, and 0.5. In the whole range, we found a perfect linear decrease of the volume represented by the blue full line. Similarly to In_2S_3, the distances are overestimated using PBE functional, explaining the higher volumes obtained in our DFT calculations. Nevertheless, the experimental and theoretical slopes of V = f(x) in the tetragonal domain are identical, as evidenced by the blue dashed line. It is also interesting to notice that by imposing the tetragonal symmetry in the DFT calculations, i.e. the ordering of V_{In}, a linear variation of the volume is expected also for $x > 0.05$, in contrast to the experiments.

This study confirms the structural evolution previously evidenced by Popovic et al. along the solid solution $(In_{1-x}Al_x)_2S_3$. This transformation from a tetragonal to a cubic structure is the same as in pure indium sulfide In_2S_3 above ~670 K,[30] but in the case of the $(In_{1-x}Al_x)_2S_3$ compounds, the driving force is the chemical disorder due to the substitution of Al for In.

3.2. ^{27}Al-NMR Study. To go further in the investigation of the structural modifications implied by the Al-substitution in the $(In_xAl_{1-x})_2S_3$ solid solution, it was necessary to consider the NMR spectroscopy. The ^{27}Al Central Transition (CT) MAS spectra are shown in Figure 3 for samples with low ($x = 0.040$) and high ($x = 0.125$ and $x = 0.185$) Al-contents. In such sulfur compounds, the ^{27}Al signal appears at higher chemical shifts with respect to oxide compounds. A similar chemical shift evolution

dx.doi.org/10.1021/cm201830e |Chem. Mater. 2011, 23, 5168–5176

Table 4. NMR Parameters of the Lines Used To Fit the ^{27}Al NMR Spectrum of $(In_{1-x}Al_x)_2S_3$ Compounds

for low Al-contents (x = 0.018, 0.029, and 0.040)					
^{27}Al NMR peak	Td1	Td2	Td3	Oh1(L)	Oh2(L)
line shape	Gauss	Gauss	Qmas1/2	Qmas1/2	amorph.
δ_{iso} (ppm)[a]	108.7 (Δ=4.2)	115.2 (Δ=3.4)	125.0	24.8	18.7
C_Q (MHz)[b]	-	-	5.0	11.7	4.3 (ΔC_Q = 0.5)
η_Q[b]	-	-	0.3	0.1	0.47

for high Al-contents (x = 0.125 and 0.185)						
^{27}Al NMR peak	Td1	Td2	Td3	Oh1(H)	Oh2(H)	Oh3(H)[c]
line shape	Gauss Lorentz	Gauss Lorentz	Qmas1/2	amorph.	amorph.	Gauss Lorentz
δ_{iso} (ppm)[a]	107.6 (Δ=5.4)	114.2 (Δ=4.7)	125.0	18.0	22.0	16.0 (Δ=7)
C_Q (MHz)[b]	-	-	5.0	11.7 (ΔC_Q = 1.3)	6.7 (ΔC_Q = 2.0)	-
η_Q[b]	-	-	0.3	0.1	0.2	-

[a] δ_{iso} is the isotropic chemical shift. Δ is the full width at half-height for Gaussian/Lorentzian line shape. [b] C_Q and η_Q are the quadrupolar coupling constant and the asymmetry parameter, respectively. ΔC_Q is the quadrupolar coupling constant dispersion for "amorphous" line shape. [c] Only observed for sample #6 (x = 0.125), possibly attributed to non long-range ordered material.

Table 5. Relative Contribution of the Lines Used To Fit the ^{27}Al NMR Spectrum of $(In_{1-x}Al_x)_2S_3$[a]

peak intensity (±5%) for low Al-contents						
sample	Td1	Td2	Td3	Oh1(L)	Oh2(L)	Td/Oh
#2 (x = 0.018)	22	0	0	37	41	22/78
#3 (x = 0.029)	21	2	3	35	39	26/74
#4 (x = 0.040)	17	0	2	41	40	19/81

peak intensity (±5%) for high Al-contents							
sample	Td1	Td2	Td3	Oh1(H)	Oh2(H)	Oh3(H)	Td/Oh
#5 (x = 0.125)	20	12	16	15	28	9	48/52
#6 (x = 0.185)	21	7	13	18	41	-	41/59

[a] (L) and (H) stand for low and high Al-content, respectively.

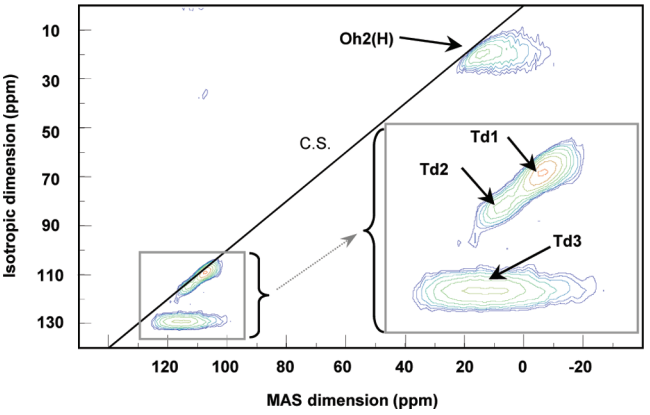

Figure 4. ^{27}Al 3Q-MAS spectrum of sample #7 (x = 0.185) evidencing the existence of 3 Td sites.

between sulfides and oxides was previously observed for ^{31}P nucleus, see for example Eckert[31] and references therein. We assigned the ^{27}Al resonances by comparison to aluminum oxides. Hence, signals around 0 and above 100 ppm are attributed to octahedral [AlS_6] and tetrahedral [AlS_4] moieties, respectively. Possible 5-fold coordination can be considered in between these two ranges. Theses assignations agree with previous investigation on the Al_2S_3 compound.[32,33] The quantitative decomposition of the spectra allows assess Al site occupancy and characterization of structural distortions around the Al substituted sites. Indeed, the ^{27}Al quadrupolar nuclei (I = 5/2) interact with the electric field gradients (EFGs) created by the surrounding charges, leading to an additional broadening in the spectrum. From the analysis of this quadrupolar broadening it is possible to extract the quadrupolar coupling constant (C_Q) and the asymmetry parameter (η_Q) values which characterize the local environment of the probed quadrupolar nucleus (i.e. nuclear spin I ≥ 1).

Let us begin by the decomposition of the Oh region for the low Al-content sample #4 (x = 0.040), as shown in Figure 3 and summarized in Table 4. The horn at −50 ppm was used to set the Oh1(L) line with the expected CT-MAS line shape, which is characteristic of the second order quadrupolar interaction under MAS conditions. This line shape will be labeled "Qmas1/2" hereafter and in Table 4. The remaining signal related to Al in 6-fold coordination resonances can be accurately described by a single "amorphous" line shape (Oh2(L) line). This line shape available inside the dm-fit program corresponds to a distribution of CT-MAS line shapes. Such an approach is more adequate for crystalline sites experiencing small structural variability than a real distribution of the EFG tensor components, which is more suited to glassy samples. The Oh region of the two other low Al-content samples #2 and #3, i.e. x = 0.018 and 0.029 respectively, can be precisely described using the 2 same lines with similar intensities (see Table 5).

In the two spectra related to high Al-contents (x = 0.125 and x = 0.185), the Oh regions look quite similar to the one of low Al-contents, as shown in Figure 3, but are featureless, suggesting more distorted octahedral sites. Taking the above decomposition as a starting point, we can propose a decomposition based on two lines (Oh1(H) and Oh2(H)), as shown in Figure 3 for sample #7 (x = 0.185). The Oh2(H) has still an "amorphous" line shape but with a larger and more distributed C_Q value. The Oh1(H) line keeps the same C_Q value than the Oh1(L) one, but an "amorphous" line shape is now needed to properly reproduce the NMR signal.

dx.doi.org/10.1021/cm201830e |Chem. Mater. 2011, 23, 5168–5176

Table 6. Selected Bond Distances, Relative Stability, and NMR Parameters of the Geometry Optimized DFT Models of $In_{63}Al_1S_{96}$[a]

model	Al−S distances (Å) [37]	relative stability (meV)	C_Q (MHz)	η_Q	^{27}Al NMR peak attribution
Oh(16h)	2.48 [2.36−2.54]	0	−12.1 (11.7)	0.0 (0.1)	Oh1(L)
Oh(8c)	2.50 [2.38−2.59]	+74	+4.3 (4.3)	0.6 (0.5)	Oh2(L)
Td(8e)	2.33 [2.31−2.34]	+170	−0.2	0.6	Td1/Td2
Td(4a)	2.33 [2.29−2.38]	+645	+4.7 (5.0)	0.4 (0.3)	Td3
Td(4a)'	2.32 [2.31−2.33]	+2797	+1.3	0.6	

[a] The last column provides the attribution of the ^{27}Al NMR lines. Experimental values of C_Q and η_Q are given in parentheses.

Finally, the Oh region of sample #6 only differs from sample #7 by an extra line (Oh3(H)) which can be clearly evidenced by spectral subtraction (Figure SI-2 in the Supporting Information). This narrow line, exhibiting no second-order quadrupolar broadening, can be associated with ^{27}Al nuclei experiencing low EFGs and then assigned to slightly distorted octahedra. Note that for sample #6, a broad signal centered at 50 ppm (marked by an arrow in Figure 3) is attributed to impurity.

The analysis of the Td region is simpler since all the spectra exhibit similar shape with only different line intensity. Particularly, in contrast to Oh region, no line broadening is observed for high Al-contents. Confident decomposition of this region can be obtained through 3Q-MAS experiment. The ^{27}Al 3Q-MAS spectrum of sample #7 (x = 0.185) shows the existence of 3 resonances in the Td region (Figure 4). Two of them (Td1 and Td2 lines) are fitted using Gaussian/Lorentzian line shape. As for the Oh3(H) line, it corresponds to ^{27}Al nuclei experiencing low EFGs and so to slightly distorted tetrahedra. The third line (Td3 line) shows a clear "Qmas1/2" line shape. Except intensities, the same parameters can be used to reproduce accurately the spectra for all the Al contents. All parameters and line intensities are gathered in Table 4 and Table 5.

3.3. DFT Calculations. While the present ^{27}Al NMR data clearly evidence that different Oh and Td sites are occupied by the Al^{3+} ions, it remains difficult to attribute without ambiguity the related NMR signals to a given crystallographic site. However, such attribution is possible based on strategies combining NMR spectroscopy with DFT calculations. In particular, DFT calculations are known for their ability to accurately estimate the crystal structures and EFGs of solids.[34,35] We recently applied such an approach to probe the Al/Si ordering in aluminosilicate compounds.[36]

In the present study, DFT geometry optimizations have been carried out in order to estimate the site preferences of Al^{3+} ions in $(In_{1-x}Al_x)_2S_3$ and the related C_Q and η_Q values. More specifically, five models have been envisioned consisting to substitute one Al^{3+} ion for one In^{3+} ion in a "$a_C \times a_C \times 3a_C$" supercell, corresponding to the formula $In_{63}Al_1S_{96}$ (x = 0.016), based on the ordered vacancy tetragonal arrangement (V(supercell) = $2 \times V_T$). These five models are labeled according to the Wyckoff positions in the $I4_1/amd$ space group: Oh(16h), Oh(8c), Td(8e), Td(4a), and Td(4a)′. It must be stressed that, in the two last cases, the Al^{3+} ion is placed on a vacant site of the In_2S_3 tetragonal phase, i.e. Td(4a), and the charge balance is achieved by removing one In^{3+} ion from an occupied site. Here we report only two extreme situations, which differ by the distance between the Al^{3+} ion and the created V_{In}, i.e. d(Al−V_{In}) = 4.7 Å and 14.4 Å in the Td(4a) and Td(4a)′ models, respectively. Such calculations are representative of low Al-content samples. The relative energies, with respect to Oh(16h) model, of the different relaxed configurations are summarized in Table 6. The energies increase in the order

$$Oh(16h) < Oh(8c) < Td(8e) << Td(4a) << Td(4a)'$$

Namely, for x = 0.016, i.e. low Al-content, the Al^{3+} substituent strongly prefers to be on octahedral sites (Oh(16h) and Oh(8c)), and in a smaller propensity on the tetrahedral Td(8e) site. The occupation of the empty Td(4a) site is less favorable, leading to highly unstable atomic arrangements.

For higher x values, the chemical disordering between In^{3+} and Al^{3+} ions appears on the tetrahedral positions, namely these two ions partly occupy all the tetrahedral sites (Td(4a) and Td(8e) sites of the $I4_1/amd$ space group) and the structure becomes cubic. It should be noticed that these two sites merge together in one tetrahedral site in the cubic structure. For simplicity, we will only use the Wyckoff labels according to the tetragonal structure.

Structural and NMR results deduced from our DFT calculations are summarized in Table 6. The first effect of the substitution of Al^{3+} ion for In^{3+} is a shrinkage of the site due to the shorter Al−S bond length compared to the In−S one. In our DFT calculations, a shortening of the M−S bond length (with M = In, Al) of 7−8% is observed when replacing In^{3+} by Al^{3+}, in very good agreement with the experimental observations. For instance, the experimental average Al−S (In−S) distances in the cubic phase of Al_2S_3 (In_2S_3) have been reported to be 2.29 (2.474) Å and 2.408 (2.614) Å, for Td and Oh sites respectively,[37] i.e. 7−8% bond length reduction from In_2S_3 to Al_2S_3. The site distortion is systematically increased in the presence of Al^{3+} ions. The site distortion indices for Oh(16h), Oh(8c), and Td(8e) sites respectively increase from 0.059, 0.053, and 0.004 to 0.073, 0.084, and 0.013 when an In^{3+} ion is replaced by Al^{3+} ion. [The distortion index (DI) of the [MS_4] and [MS_6] polyhedra is defined as DI = $(d_{max} - d_{min})/<d_{M\text{-}S}>$, where d_{max} and d_{min} refer to the maximum and the minimum M−S distances of the polyhedra and $<d_{M\text{-}S}>$ to the average M−S distance of the polyhedra. The distortion index is a measure of the extent of the asymmetry of each polyhedron; the larger the distortion index, the larger extent of asymmetry of the polyhedron.]

Interestingly, for the two more favorable sites, i.e. Oh(16h) and Oh(8c), the resulting NMR simulations could be easily attributed to the measured NMR lines Oh1(L) and Oh2(L), respectively. For the tetrahedral sites, the experimental line deconvolution cannot give accurate C_Q and η_Q values. However, from 3Q-MAS spectra, it could be evidenced that the C_Q values related to the tetrahedral sites are smaller than 2 MHz, which could correspond to our DFT C_Q values for Td(8e) and Td(4a)′ models, i.e. −0.2 and +1.3 MHz, respectively. An unambiguous attribution of the Td1 and Td2 lines is then not achievable from

dx.doi.org/10.1021/cm201830e |Chem. Mater. 2011, 23, 5168–5176

Table 7. Atomic Coordinates and Equivalent Isotropic Displacement Parameters for $(In_{0.97}Al_{0.03})S_3$ and $(In_{0.89}Al_{0.11})S_3$ Determined Using the Single-Crystal XRD Data

atom	site	x	y	z	U_{eq} (Å^2)	sof[a]	bond valence
$(In_{0.97}Al_{0.03})S_3$							
In1/Al1	8c	0	0	0	0.0171(2)	0.97/0.03	3.06
In2/Al2	16h	0	−0.01933(5)	0.33248(1)	0.0161(1)	0.97/0.03	3.00
In3/Al3	8e	0	0.25	0.20459(1)	0.0120(1)	0.97/0.03	3.00
S1	16h	0	−0.0075(2)	0.25088(6)	0.0135(4)	1	2.12
S2	16h	0	0.0099(2)	0.07833(6)	0.0152(4)	1	1.86
S3	16h	0	0.0220(2)	0.41324(6)	0.0115(3)	1	2.05
$(In_{0.89}Al_{0.11})S_3$							
In1/Al1	16d	0.5	0.5	0.5	0.0269(3)	0.901(4)/ 0.099(-)	3.03
In2/Al2	8a	0.125	0.125	0.125	0.0147(4)	0.572(-)/ 0.095(-)	3.07
S	32e	0.2568(2)	0.2568(2)	0.2568(2)	0.0193(3)	1	2.03

[a] Site occupancy factor. For $(In_{0.97}Al_{0.03})S_3$ sof were fixed according the Al-content (x = 0.03, from the unit cell parameters) and the Td-Oh Al-distribution (close to 25−75, from the NMR measurements).

the present analysis. However, our DFT calculations have evidenced that the Td(4a)′ model is highly unstable (+2.6 eV) compared to the Td(8e) model. Then we could attribute the Td1 and Td2 NMR lines to Al^{3+} ions occupying two different Td(8e) sites, having small differences in their local environment, related to the surrounding Al^{3+} ions and V_{In}.

Finally, although the occupation of the Td(4a) site by an Al^{3+} ion is less favorable for low Al-contents, the Td(4a) model leads to C_Q and η_Q values very close to the Td3 NMR line values. Thus, the present DFT result allows the attribution of the Td3 NMR line to the Td(4a) site by an Al^{3+} ion close to an indium vacancy. It should be stressed that the Td3 line is only observed for high Al-contents. Although the present calculations are done in a "highly diluted limit", with x = 0.016, their use to interpret the NMR data for higher Al-content is justified by the local nature of the NMR probe.

3.4. Single Crystal Structure Investigations. From the present combination of ^{27}Al NMR experiments and DFT calculations, a precise understanding of the local structure around the Al^{3+} ions in $(In_{1-x}Al_x)_2S_3$ has been deduced. Based on this knowledge, we considered the single crystal refinements of our $(In_{1-x}Al_x)_2S_3$ samples. Among the large set of prepared samples it was possible to select two single crystals suitable for X-ray structure refinement. The best selected single crystal of sample #4 was twinned along the [601] row axis of the tetragonal unit cell and was not of high quality for X-ray diffraction. The examination of the extinction conditions leads to the use of the same $I4_1/amd$ space group as for β-In_2S_3. The crystal structure investigation was quite hard because of the very low Al-content. Indeed, it is readily apparent that the distribution of Al on at least 3 cationic sites could be quite complex leading to too many possible configurations which cannot be distinguished through the structure reliability factors analysis. Then, the Al-content was fixed to x = 0.03 according to the measured value of the unit cell volume (see Figure 2). This value is quite close to that obtained from the WDS analyses on the corresponding powder sample (x = 0.04). In addition, the octahedral/tetrahedral occupancy ratio was fixed to the value determined from the corresponding ^{27}Al-NMR spectrum (Td/Oh close to 25/75). Finally, the reliability factors converged to R/Rw(obs) = 3.89/8.54 for 1922 observed reflections and 36 refined parameters. The corresponding Fourier-difference map is featureless (+1.61/−1.32 e/Å^3).

The third investigated crystal structure was for an Al-content close to x = 0.125 (sample #6). As in the previous case, the actual composition, x = 0.11, was estimated from the value of the unit cell volume (see Figure 2) measured on the single crystal. According to both the powder and single crystal X-ray diffraction studies the symmetry of this compound is found to be cubic. The structure determination has been performed in the *Fd*-3*m* space group. The site occupancy factors of Al on both sites Oh(16d) and Td(8a) were constrained according to the whole Al-content in the structure (x = 0.11). In the first step, the refinement was performed using the Al-distribution deduced from the NMR measurements (Oh/Td = 52/48). The reliability factor converged to R_{obs} = 5.62%, and the examination of the Fourier-difference map revealed a residual peak of 3.66 e$^-$/Å^3. In the second step, the Al-distribution was refined, leading to a significant improvement of the refinement (R_{obs} = 4.73%) and to a featureless Fourier-difference map (+2.66 /-2.45 e$^-$/Å^3). The Al percentage on the tetrahedral site converged to 32% which is quite different than the one determined from the NMR spectrum (48%). As indicated in the NMR result section, the sample #6 seems to behave strangely compared to the other samples (Oh extra line). This powder sample could contain a part of non long-range ordered materials and thus, the single crystal could be of composition a little bit different than that of the corresponding powder. It is worth noticing that the structural Oh/Td ratio for sample #6 is compatible with the slight evolution observed from the NMR study (see Table 4).

The final atomic coordinates and equivalent isotropic atomic displacement parameters for both structures are given in Table 7. It should be noticed that, for the highest Al-content, it was impossible to find single crystal suitable for X-ray diffraction. It seems that the crystallization process is getting worse and worse as the Al-content increases.

3.5. Discussion. The present investigation of the $(In_{1-x}Al_x)_2S_3$ compounds, based on the combination of X-ray diffraction, NMR spectroscopy, and DFT modeling, demonstrates without ambiguity that the substitution of aluminum for indium in In_2S_3 leads to a complex solid solution. The structure is more and more disordered when aluminum content increases leading to a transition from the tetragonal structure (ordered vacancy compound) to the disordered cubic structure. The coupling of the NMR experiments and DFT simulations leads to the attribution of the main NMR lines. In particular, the lines Oh1,

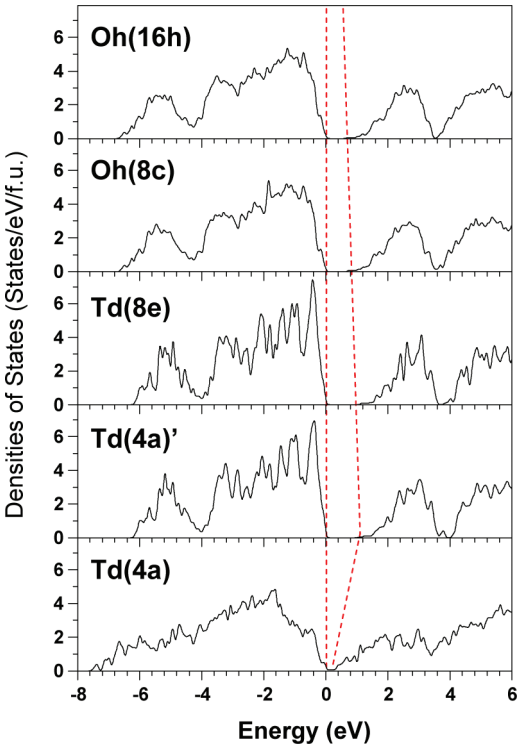

Figure 5. DFT total density of states for the five studied models using a supercell with the formula $In_{63}Al_1S_{96}$ ($x = 0.016$). The red dashed lines correspond to the band gaps.

Oh2, and Td3 are attributed to the Oh(16h), Oh(8c), and Td(4a) (with a short Al−V_{In} distance) sites, respectively. The lines Td1 and Td2 appear to be related to the occupation of the Td(8e) site, as evidenced by their small C_Q values, and differ by their local environment (proximity of other Al^{3+} ions and indium vacancies). It clearly appears that the octahedral sites are preferentially occupied for low Al-contents, both from the NMR peak intensities (Table 5) and the relative energies of the DFT models (Table 6). More specifically, a Td/Oh ratio of about 20/80 is found for the low Al-contents, while for high Al-contents this ratio is about 50/50. Thus from low to high Al-contents, the structure undergoes an important modification, namely the Al^{3+} distribution is changed leading to the occupation of as many tetrahedral sites as octahedral ones. In addition, the Td(4a) sites becomes occupied in the rich-Al compounds.

The present structural analysis could be really helpful in better understanding the evolution of the optical properties in $(In_{1-x}Al_x)_2S_3$ as a function of x, namely the nonlinear increase of E_g when x is raised, with E_g values that saturate to about 2.2 eV. It is important to understand what structural factors govern this optical gap evolution.

Figure 5 shows the total densities of states (DOS) corresponding to the five envisioned models for $x = 0.016$, after atomic relaxation. As expected, the band gaps are underestimated, but it clearly appears that only for the Td(4a) model a significant reduction of the band gap is observed. In this model an Al^{3+} defect is located on a Td(4a) site locally stabilized by the removal of an In^{3+} ion on the nearest site, i.e. a Td(8e) site (red tetrahedron in Figure 1). From our combined "XRD, NMR and DFT" approach, it appears that such a situation is highly probable for high Al-contents. In particular, it corresponds to the appearance of the Td3 line, attributed to the Td(4a) model, for $x = 0.125$ and 0.185, with 16% and 13% respectively of Al^{3+} ions in this situation.

According to the present band gaps estimations, it is most likely that the band gap saturation with x in $(In_{1-x}Al_x)_2S_3$ is related to the occupation of the Td(4a) site. We verified this last observation by doing a "DFT experiment", namely we have estimated the band gap evolution in a $(In_{1-x}Al_x)_2S_3$ series with $x = 0$, 0.125, 0.25, 0.375 and 0.5, i.e. using the relaxed structures previously described in part 3.1. In all these structures, the Al^{3+} ions was positioned in the Oh(16h) site. The resulting band gap progressively increases when x goes from 0 to 0.5, and no saturation effect is observed (see Figure SI-3 in the Supporting Information).

4. CONCLUSION

In this work, we have characterized for the very first time the aluminum distribution in $(In_{1-x}Al_x)_2S_3$ ($0 \le x \le 0.185$) using a strategy combining X-ray diffraction, ^{27}Al-NMR spectroscopy, and DFT geometry optimization. It is remarkable that for low Al contents, the selective nature of the NMR spectroscopy is a real asset. As shown above it allows both the discrimination between Al coordinations and the quantitative determination of the Al sites occupancies. In particular, the comparison of the experimental and theoretical ^{27}NMR quadrupolar constant values leads to an unambiguous identification of the nature of the Al-sites in $(In,Al)_2S_3$. The occupation of a new tetrahedral site (Td(4a)) has been evidenced for high Al-content, leading to a band gap decrease. The analysis of the DFT densities of states shows that a control of the Al-site occupation is a prerequisite to overcome the band gap saturation experimentally observed for $x > 0.03$. Therefore, to obtain efficient alternative buffer layer for thin-film solar devices, it would be interesting to seek Al-substituted In_2S_3 materials in which all the Td(4a) sites will be previously filled by an extra cation, such as Cu^+ or Na^+.

■ ASSOCIATED CONTENT

Supporting Information. Crystallographic information (CIF) of In_2S_3, $(In_{0.97}Al_{0.03})_2S_3$, and $(In_{0.875}Al_{0.125})_2S_3$; full pattern matching plot for sample #3; ^{27}Al signal difference between the signatures of samples #6 and #7 in the Oh region. DOS for the hypothetic $(In_{1-x}Al_x)_2S_3$ series with $x = 0$, 0.125, 0.25, 0.375, and 0.5. This material is available free of charge via the Internet at http://pubs.acs.org.

■ AUTHOR INFORMATION

Corresponding Author

*E-mail: Alain.Lafond@cnrs-imn.fr (A.L.), Xavier.Rocquefelte@cnrs-imn.fr (X.R.).

■ ACKNOWLEDGMENT

Yann Borjon Piron and Erik Elkaim are gratefully acknowledged for the help provided during the WDS measurements and data collection for X-ray diffraction on the beamline CRISTAL at synchrotron Soleil, respectively.

■ REFERENCES

(1) Jackson, P.; Hariskos, D.; Lotter, E.; Paetel, S.; Wuerz, R.; Menner, R.; Wischmann, W. Powalla M. *Progress in Photovoltaics: Research and Applications* 2011, 19, doi: 10.1002/pip.1078.

(2) Abou-Ras, D.; Kostorz, G.; Strohm, A.; Schock, H.-W.; Tiwari, A. N. *J. Appl. Phys.* **2005**, *97*, 123512/123511–123512/123517.
(3) Allsop, N. A.; Schoenmann, A.; Muffler, H.-J.; Baer, M.; Lux-Steiner, M. C.; Fischer, C.-H. *Prog. Photovoltaics* **2005**, *13*, 607–616.
(4) Buecheler, S.; Corica, D.; Guettler, D.; Chirila, A.; Verma, R.; Mueller, U.; Niesen, T. P.; Palm, J.; Tiwari, A. N. *Thin Solid Films* **2009**, *517*, 2312–2315.
(5) Marlein, J.; Decock, K.; Burgelman, M. *Thin Solid Films* **2009**, *517*, 2353–2356.
(6) Verma, R.; Datta, D.; Chirila, A.; Guettler, D.; Perrenoud, J.; Pianezzi, F.; Mueller, U.; Kumar, S.; Tiwari, A. N. *J. Appl. Phys.* **2010**, *108*, 074904/074901–074904/074910.
(7) Rehwald, W.; Harbeke, G. *Phys. Chem. Solids* **1965**, *26*, 1309–1324.
(8) Kambas, K.; Anagnostopoulos, A.; Ves, S.; Ploss, B.; Spyridelis, J. *Phys. Stat. Sol. B* **1985**, *127*, 201–208.
(9) Ho, C. H.; Wang, Y. P.; Chan, C. H.; Huang, Y. S.; Li, C. H. *J. Appl. Phys.* **2010**, *108*, 043518–043518.
(10) Barreau, N.; Marsillac, S.; Albertini, D.; Bernede, J. C. *Thin Solid Films* **2002**, *403−404*, 505–509.
(11) Schulte-Kellinghaus, M.; Krämer, V. *Acta Crystallogr.* **1979**, *B35*, 3016–3017.
(12) Couzinié -Devy, F.; Arzel, L.; Barreau, N.; Guillot-Deudon, C.; Harel, S.; Lafond, A.; Kessler, J. *J. Cryst. Growth* **2010**, *312*, 502–506.
(13) Rampersadha, N. S.; Ventera, A. M.; Billingb, D. G. *Physica B* **2004**, *350*, e383–e385.
(14) Steigmann, G. A.; Sutherland, H. H.; Goodyear, J. *Acta Crystallogr.* **1965**, *19*, 967–971.
(15) Adenis, C.; Olivier-Fourcade, J.; Jumas, J. C.; Philippot, E. *Rev. Chim. Miner.* **1987**, *24*, 10–21.
(16) Hahn, H.; Klingler, W. *Z. Anorg. Chem.* **1949**, *260*, 97–109.
(17) Likforman, A.; Guittard, M.; Tomas, A.; Flahaut, J. *J. Solid State Chem.* **1980**, *34*, 353–359.
(18) Popovic, S.; Grzeta-Plenkovic, B.; Etlinger, B. *J. Appl. Crystallogr.* **1982**, *15*, 107–111.
(19) Petricek, V.; Dusek, M.; Palatinus, L. 2006, Jana2006. The crystallographic computing system.
(20) Goodyear, J.; Steigmann, G. A. *Proc. Phys. Soc., London* **1961**, *78*, 491–495.
(21) Amoureux, J.-P.; Fernandez, C.; Steuernagel, S. *J. Magn. Reson., Ser. A* **1996**, *123*, 116–118.
(22) Massiot, D.; Fayon, F.; Capron, M.; King, I.; Le Calve, S.; Alonso, B.; Durand, J.-O.; Bujoli, B.; Gan, Z.; Hoatson, G. *Magn. Reson. Chem.* **2002**, *40*, 70–76.
(23) Kresse, G.; Furthmuller, J. *Phys. Rev. B* **1996**, *54*, 11169–11186.
(24) Blaha, P.; Schwarz, K.; Madsen, G.; Kvasnicka, D. Luitz, J. 2001, WIEN2k, An Augmented Plane Wave + Local Orbitals Program for Calculating Crystal Properties.
(25) Perdew, J. P.; Burke, K.; Ernzerhof, M. *Phys. Rev. Lett.* **1996**, *77*, 3865–3868.
(26) Blochl, P. E. *Phys. Rev. B* **1994**, *50*, 17953–17979.
(27) Methfessel, M.; Paxton, A. T. *Phys. Rev. B* **1989**, *40*, 3616–3621.
(28) Monkhorst, H. J. P., J. D. *Phys. Rev. B* **1976**, *13*, 5188–5192.
(29) Palacios, P.; Aguilera, I.; Sanchez, K.; Conesa, J. C.; Wahnon, P. *Phys. Rev. Lett.* **2008**, *101*, 046403.
(30) van Landuyt, J.; Amelinckx, S. *Phys. Status Solidi B* **1969**, *31*, 589–600.
(31) Eckert, H. *Prog. Nucl. Magn. Reson. Spectrosc.* **1992**, *24*, 159–293.
(32) Jung, W.-S.; Ahn, S.-K. *Mater. Lett.* **2000**, *43*, 53–56.
(33) Martin, S. M.; Sills, J. A. *J. Non-Crystal. Sol.* **1991**, *135*, 171–181.
(34) Blaha, P.; Schwarz, K.; Herzig, P. *Phys. Rev. Lett.* **1985**, *54*, 1192–1195.
(35) Gervais, C.; Profeta, M.; Babonneau, F.; Pickard, C. J.; Mauri, F. *J. Phys. Chem. B* **2004**, *108*, 13249–13253.
(36) Rocquefelte, X.; Clabau, F.; Paris, M.; Deniard, P.; Le Mercier, T.; Jobic, S.; Whangbo, M.-H. *Inorg. Chem.* **2007**, *46*, 5456–5458.
(37) Range, K. J.; Huebner, H. J. *Z. Naturforsch., B: J. Chem. Sci.* **1973**, *28*, 353–355.
(38) Brown, I. D.; Altermatt, D. *Acta Crystallogr.* **1985**, *B41*, 244–247.
(39) Brese, N. E.; O'Keeffe, M. *Acta Crystallogr.* **1991**, *B47*, 192–197.